Microelectronics Reliability 123 (2021) 114219

Contents lists available at ScienceDirect

Microelectronics Reliability

journal homepage: www.elsevier.com/locate/microrel

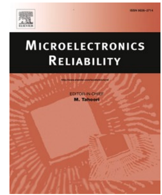

Theoretical examination of thermo-migration in novel platinum microheaters

Lado Filipovic

Institute for Microelectronics, Technische Universität Wien, Gußhausstraße 27-29/E360, Vienna 1040, Austria

A R T I C L E I N F O

Keywords:
Thermo-migration
Electro-migration
Platinum
Microheater
Semiconductor metal oxide
Gas sensors
Modeling and simulation

A B S T R A C T

Conductometric gas sensors based on SMO films must be heated to temperatures up to 550 °C in order to initiate the molecular adsorption process at the SMO film's surface. Very often platinum is used as the microheater material. The long-term reliability of these devices are primarily associated with the mechanical stability of the micro-electro-mechanical systems (MEMS) structures used to hold the microheater suspended and thermally isolated from other integrated components, such as analog and digital circuitry. However, previous studies have shown that that electro-migration and thermo-migration phenomena could potentially exacerbate the stress build-up in platinum microheaters and contribute to their eventual failure. In this manuscript we propose a means to quantify the impact of vacancy transport on stress build-up in two novel microheater designs under electro-migration and thermo-migration phenomena. The first design is aimed at improved temperature uniformity and the second is aimed at microheater array operation, taking advantage of high temperature gradients to simultaneously provide multiple temperatures at different sensor locations. Our analysis shows that the thermo-migration force is much higher than the electro-migration force, meaning that the high thermal gradients in these devices contribute far more to vacancy transport than the atom transport induced by the electron wind. Furthermore, we calculate that our proposed designs are highly resistant to failure due to vacancy migration by calculating the mean-time-to-failure to be on the order of 10^{15} seconds under typical operating conditions.

1. Introduction

Several different types of sensors rely on the integration of a hotplate or heater element in order to enable their primary sensing functionality. Some typical examples of these are SMO chemoresistive gas sensors [1–3], infrared emitters for NDIR optical gas sensors [4–6], and thermoelectric infrared microbolometers [7,8]. SMO sensors rely on a redox reaction on its surface, which requires heating the sensitive film to temperatures between 200 °C and 550 °C, while NDIR gas sensors require temperatures above 600 °C to provide a reasonably strong IR signal [6,9].

1.1. Background

To allow for the necessary sensor heating a microheater or microhotplate is integrated within the device, underneath the sensing film. To ensure proper integration with analog and digital electronics and to allow for cost-effective fabrication, the integration of the microheater and SMO film with CMOS fabrication techniques is highly desired [10]. This means that the choice of material is somewhat limited and quite commonly, the microheater material is Pt [11] or W [12]. Tungsten, while being practically resistant to EM and TM phenomena, tends to form an oxide when exposed to air at high temperatures, requiring a capping layer [13]. Platinum, on the other hand, is very stable, has a linear temperature response, and is resistant to oxidation for a broad range of operating temperatures [14]. Nevertheless, there is some experimental evidence of detrimental EM or TM forces in thin platinum films and lines, leading to atom migration [15,16]. Therefore, it is important to ensure that newly proposed platinum microheater designs will not experience early failure due to these effects. The EM and TM effects in microheaters very difficult to qualify and fully understand experimentally since there are always several effects influencing the different material stacks at high operating temperatures, including diffusion of atoms from the adhesion layer, thermal expansion, membrane deflection and relaxation, and cracking and delamination [17–19]. Ultimately, when we propose a new platinum-based microheater design, we need a means to ensure that it will be resistant to potential EM and TM failure.

E-mail address: filipovic@iue.tuwien.ac.at.

https://doi.org/10.1016/j.microrel.2021.114219
Received 26 March 2021; Received in revised form 28 May 2021; Accepted 23 June 2021
Available online 12 July 2021
0026-2714/© 2021 The Author. Published by Elsevier Ltd. This is an open access article under the CC BY license (http://creativecommons.org/licenses/by/4.0/).

The heating of a metallic microheater is induced by the Joule effect, which requires the application of elevated current densities. The elevated current densities and temperatures are synonymous with potential failure in metallic lines due to the induced vacancy transport and accumulation, resulting in stress [20–22]. The most common theoretical studies involving vacancy-induced stress are based on EM in copper interconnects for advanced CMOS devices [23–25]. For these studies, the experimental measurements and simulations are performed at elevated temperatures (around 300 °C) in order to accelerate the vacancy transport since at room temperature, the time to failure can be on the order of months or years. Due to this factor, the TM component inducing vacancy transport is often ignored, while it is well known that TM can exacerbate the vacancy transport and cause early failure [22]. Since copper interconnects are generally operated near room temperature and high thermal gradients are much less common than high current densities, it is appropriate to ignore the TM component in these devices and concentrate primarily on EM as the principal driving force behind vacancy migration. However, this is not likely to be the case for microheaters. A recent work on a typical meander microheater has demonstrated that TM should not be ignored when analyzing these structures, as the TM component can be higher than the EM component therein [26]. Furthermore, the potential for EM and TM induced failure has been experimentally shown in thin platinum films [15,16]. Therefore, in this manuscript, we study the EM and TM phenomena in two recently proposed microheater designs, which are aimed at low-power and microheater array applications [11]. This further allows quantifying the impact of EM- and TM-induced stresses in comparison to the commonly studied thermo-mechanical failure mechanism [19,27].

1.2. Modeling the mechanical stability of gas sensor microheaters

One of the primary challenges in designing gas sensor microheaters is ensuring their mechanical stability. The stacked membrane structures can suffer from several types of thermally induced stresses during fabrication and operation [27]. To model these properly, one must analyze the internal stress accumulation in the sensor microheater and the membrane layers, including SiN and SiO 2. The stress could directly impact the generation of crystalline defects, poor adhesion between layers, and formation of undesirable surface growths [19]. Furthermore, the build-up of stress in very small regions can lead to initial cracking and delamination, ultimately resulting in complete device failure [28]. For this reason, modeling stress in these structures has become essential, especially due to the elevated temperatures involved in the fabrication and operation of these devices. These simulations are most often performed using FEM tools in order to calculate essential parameters for the verification of the thermal performance, including the temperature distribution, thermal response time, temperature gradient, heat losses, and heat exchange between the sensor and environment [19]. Measuring these parameters without the help of FEM tools may be challenging and is in some cases impossible, especially if the temperature is changing quickly or needs to be measured inside the materials themselves.

The thermal strain ε_{th} builds up due to a change in temperature and is governed by

$$\varepsilon_{th} = \alpha(T - T_0), \tag{1}$$

where α is the coefficient of thermal expansion for the material and $T - T_0$ represents the change in temperature which leads to the build-up of thermal strain. In addition to the thermal strain, the metal microheater film may suffer from intrinsic stresses which arise during the film's growth. The intrinsic stress has been attributed to several phenomena [19] including grain growth [29], grain coalescence [30], the vacancy annihilation [31], annealing [32], insertion of excess atoms [33,34], or Misfit stress [35,36]. The intrinsic stress is very difficult to measure and is therefore commonly calculated by subtracting the thermal stress from the as-measured stress at room temperature after film deposition [19,37]. Alternatively, there are models which can be used to estimate this stress, such as the Volmer-Weber growth model, commonly applied to study stress during the growth of thin metal films [37,38].

While thermo-mechanical simulations are most appropriately modeled using FEM tools, electro-thermal simulations have also been studied using other techniques. One common method is the Cauer network model, which discretizes the entire sensor geometry and assigns to each discretized element a thermal resistor and thermal capacitor which take into consideration the various heat losses, including conductive, convective, and radiation [39,40]. The combined geometry is then modeled using a simple Spice-like circuit which helps to study the transient electro-thermal behavior and power-temperature relationship without the need for FEM tools [41].

Once the stress is known, the important question to answer is whether fracture can occur. To simulate this, a fracture parameter model needs to be determined in such a film stack in order to be able to simulate the crack driving force [42]. In principle, a crack with an initial length l_0 will extend if the CDF exceeds the crack growth resistance R_c [43]. The resistance R_c depends on several material parameters, including the fracture toughness and plasticity, as well as on the geometry [19]. There are several regimes which can be used to represent fracture mechanics, which depend on the material involved. These are LEFM and EPFM or NLFM [44]. LEFM applies if the plastic deformation during crack growth is zero or limited, while EPFM applies when the body experiences significant plastic deformation. The equations which must be solved to calculate the impact of the stress near a crack on its propagation in time are summarized by Coppeta et al. [19].

2. Platinum microheaters for SMO gas sensors

The two platinum microheater designs whose EM and TM response we want to study here were initially proposed by Lahlalia et al. in [11]. The first design (D1) concentrated on reducing the operating power while providing a highly uniform sensing area using a dual-hotplate design and the second design (D2) was aimed at providing a microheater array, where a single device simultaneously provides two different temperatures. In this study, our aim is to understand the impact of TM and EM on the proposed microheaters' reliability, whether these phenomena should be investigated when novel designs are presented, and whether improving temperature uniformity can help in improving the sensors' lifetimes. The studied designs both contain a 200 nm-thick platinum microheater, with a titanium tungsten (TiW) dielectric, on a SiO_2/SiN/SiO_2 membrane stack with thicknesses 500 nm/300 nm/500 nm. The MEMS membrane is released by etching an air cavity below it, while it is held up with the help of four or three suspension beams, for designs D1 and D2, respectively. Finally, an additional 300 nm SiO_2 isolation is deposited on top of the microheater, followed by the sensing film (SnO_2) and the platinum electrodes, once again with a TiW dielectric below it to ensure good adhesion to SiO_2. The two designs are given in Fig. 1 where the first design (D1) provides 300 °C to a circular sensor with a 180 m diameter, while consuming a modest 7.3 mW DC power and a temperature variation from center to edge of about 4%, depicted in Fig. 2(a). The high temperature uniformity was shown to lead to a faster response and higher sensitivity of SMO sensors in previous studies [1].

For SMO sensors, the major hurdle to overcome is selectivity and specificity since it is difficult to ascertain precisely which gas molecule adsorbs at the surface, causing a change in its conductance [10]. The introduction of specificity is commonly achieved using a sensor array, where each sensor is fabricated with an improved selectivity towards a particular gas molecule [45]. The array is commonly designed by using different sensing films or by introducing different dopants for different sensor chips, then connecting these together using a microcontroller [46]. However, the sensor arrays are bulky and require too much power to be applicable for integrated and portable technologies. Therefore, for

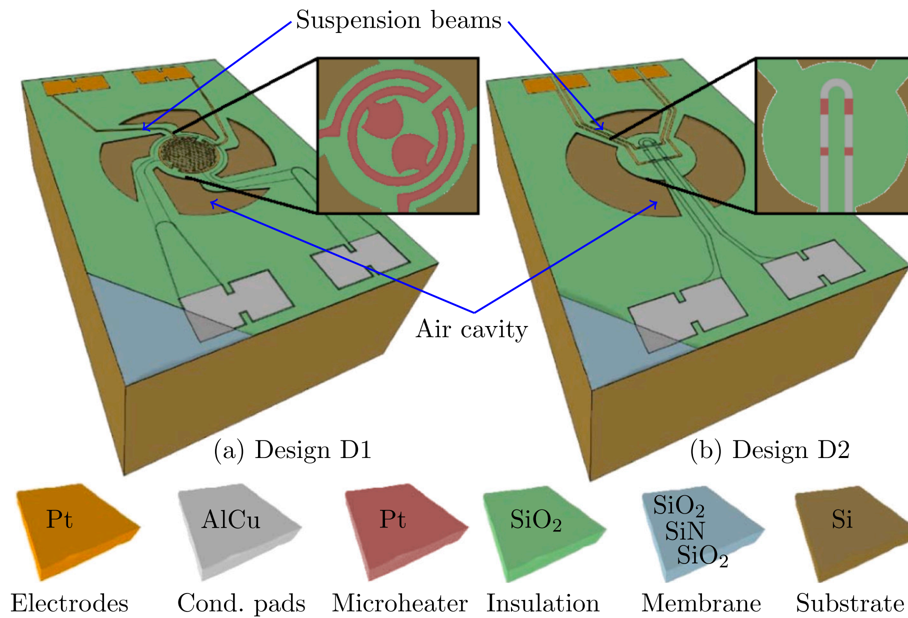

Fig. 1. SMO designs and their microheater shape (inset) for (a) Design D1: A dual-hotplate design for a highly uniform-temperature microheater and (b) Design D2: A microheater array. Note that the Pt microheater layer in (b) is also deposited underneath the AlCu line in the microheater shown in the top right inset.

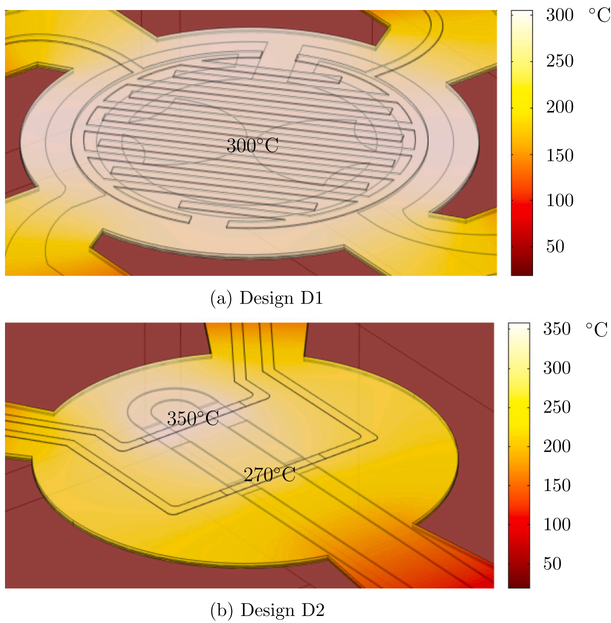

Fig. 2. Operational temperature distribution of the designs presented in Fig. 1 with (a) design D1: dual-hotplate and (b) design D2: microheater array.

our second design (D2), we proposed replacing the sensor array with a microheater array, whereby the inherent temperature non-uniformity in a microheater is used to provide a highly efficient sensor array, depicted in Fig. 1(b). Each combination of sensing film and target gas has an optimal operating temperature and by providing multiple temperatures on the same sensing film, selectivity can be introduced using more efficient, less power-hungry designs [11]. The presented design achieves simultaneous temperatures of 350 °C and 270 °C while dissipating only 8.8 mW of DC power (Fig. 2b). However, our main concern with this design is the presence of high temperature gradients therein, which could lead to a significant increase in TM-induced strain and early failure [22], which we study in this manuscript. For both presented designs, we have designed the microheater to avoid sharp corners and edges which can lead to current crowding and increased EM effects, as was shown to be the case for the meander design [26].

3. Vacancy transport in platinum

Atoms migrate inside a metal layer due to three primary driving forces, EM, TM, and SM. The physics behind these forces and a model which is applied to simulate their behavior inside platinum microheaters are described here.

3.1. Physics of vacancy transport

The driving force behind EM and TM induced failure stems from the accumulation of vacancies leading to void formation and the accumulation of atoms leading to hillock formation. These two effects lead to the generation of increased tensile and compressive stresses, high stress gradients, and ultimately SM. The stresses can either cause cracking in the film or they can ultimately lead to the formation of a void which grows to induce an open-circuit failure [47]. The change in the vacancy concentration C_v in time t is given by summing the effects of the EM- and TM-induced vacancy flux $\vec{J}_v$ and the vacancy generation and annihilation G taking place at grain boundaries and material interfaces. A further effect caused by the induced stress gradient $\nabla\sigma$ must also be included, commonly referred to as SM. Generally, it is assumed that the stress gradients inside the as-deposited film is minimal, therefore the factors which kick-start the vacancy transport are EM and TM. The induced stress due to these two factors increases over time, ultimately leading to the SM component being the most pronounced in the later stages of failure. The equation which governs the change in vacancy concentration over time is given by

$$\frac{\delta C_v}{\delta t} = -\nabla\cdot\vec{J}_v + G, \quad (2)$$

where the vacancy flux is related to diffusivity D_v which governs the EM, TM, and SM fluxes, given by

$$\overleftarrow{J_{v,EM}} = -\frac{D_v C_v}{kT} eZ^* \nabla\varphi, \quad \text{where} \nabla\varphi = \rho \overrightarrow{j}$$

$$\overleftarrow{J_{v,TM}} = \frac{D_v C_v}{kT^2} Q^* \nabla T \tag{3}$$

$$\overleftarrow{J_{v,SM}} = -\frac{D_v C_v}{kT} \Omega \nabla\sigma,$$

The total vacancy flux is given by sum of the vacancy concentration gradient ∇C_v and these components, given by

$$\overrightarrow{J_v} = -D_v \left[\nabla C_v + \frac{C_v}{kT} \left(eZ^* \nabla\varphi - \frac{Q^*}{T} \nabla T + f\Omega\nabla\sigma \right) \right], \tag{4}$$

where k is Boltzmann's constant, T is temperature, e is elementary charge, φ is electric potential, ρ is resistivity, $\overrightarrow{j}$ is current density, and σ is hydrostatic stress. The other parameters used in the model, their meaning, and their measured values for platinum thin films are provided in Table 1. These parameters were collected from a literature study, as noted in the table. For a metal such as copper, the effective valence Z^* is a relatively high negative number (-5) [48] while for platinum, Z^* is a much lower positive value (0.3) [49], suggesting that EM is less effective in platinum films.

Regions of the film which experience a high current density j and electric field $\Delta\varphi$ increase their temperature due to Joule heating, which is another reason why sharp edges and corners should be avoided. Therefore, the direction of the temperature gradient ΔT is the same as the direction of the electric field $\Delta\varphi$. The TM force moves atoms from hot to cool areas along high temperature gradients which is where they tend to accumulate and cause high compressive stress. In platinum, the EM force is in the opposite direction, due to the positive valence value. As shown in Eq. (4), the EM component ($eZ^* \nabla \varphi$) is opposite in sign to the TM component ($Q^* \nabla T/T$) when $Z^*>0$, as is the case for platinum. Therefore, we can expect that the effects of EM and TM will be opposite since vacancy accumulation induces tensile stress and atom accumulation induces compressive stresses. Furthermore, the parameter of atom diffusivity D_v also depends on the induced stress σ [50,51] as defined by

$$D_v = D_{v0} exp\left(\frac{\Omega\sigma - E_a}{kT} \right). \tag{5}$$

The vacancy generation/annihilation term G from Eq. (2) is defined by the Rosenberg-Ohring function [52] given as

$$G = \frac{1}{\tau}(C_v - C_{v0}). \tag{6}$$

When an atom is exchanged by a vacancy, the effective volume change leads to the build-up of strain ε [58]. The vacancy-induced strain causes a stress σ to form, determined by Hooke's law, assuming elastic material properties [59]. While some of the applied simulation temperatures would suggest the need to introduce plasticity to the Pt film [60,61], the goal of this investigation is to study the effects as they would be at normal operating temperatures, up to 350 °C, which can still be described as mainly elastic while plasticity is observed above about 600 °C [61,62]. Once the induced stress reaches a critical threshold σ_c, the metal layer will either crack or a void will form which then proceed to grow, increasing the line resistance and eventually causing an open circuit failure [63]. The dependencies between the different forces acting on the metal atoms (EM, TM, and SM), their driving forces (j, T, ΔT, σ, and $\Delta\sigma$), and the vacancy transport parameters (C_v and D_v), as discussed in the above equations, are visually represented in Fig. 3.

Table 1
Parameters used for the simulation of vacancy-induced stress build-up and failure in platinum.

Symbol	Description	Value	Ref.
C_{v0}	Equilibrium vacancy concentration	1.07×10^{16} cm^{-3}	[53]
D_{v0}	Diffusivity pre-exponential factor	0.22 cm^{2}s^{-1}	[54]
E_a	Activation energy for diffusion	2.89 eV	[54]
f	Vacancy relaxation factor	0.5	[55]
Ω	Atomic volume of Pt	1.51×10^{-29} m^3	–
Q^*	Heat of transport	0.68 eV	[56]
τ	Vacancy relaxation time	200 ms	[57]
Z^*	Effective valence	0.3	[49]

3.2. Modeling vacancy migration in platinum

The complexity of modeling vacancy transport becomes clear after observing the interplay between different parameters in Eqs. (2)–(6), noted in Fig. 3. In the case of copper interconnects, EM simulations and experiments are performed under accelerated conditions, meaning that a very high current density and a high uniform temperature are applied [48,16,25]. Using Black's equation, the behavior at accelerated conditions can be extrapolated back to operating conditions to find the MTTF [64]. To simulate EM, TM, and SM in microheaters, only an increased current density is applied and a uniform temperature is not prescribed, but rather it is solved for using Joule heating, represented by the arrow from j to $T/\Delta T$ in Fig. 3. This allows for the simulation of naturally forming temperature gradients in the microheater layer, which is commonly ignored when performing EM simulations in, e.g., copper interconnects [25,65], but is essential in microheaters with a poor temperature uniformity. The general flowchart to simulating these phenomena and solving vacancy transport and the induced mechanical stress is given in Fig. 4.

3.2.1. The electro-thermal problem

The current density and temperature, as well as their gradients, inside the metal film must be determined. This part of the simulation is performed on the complete 3D structures given in Fig. 1 with the assumption that the surrounding temperature is 20 °C. The temperature coefficient of resistance for platinum was fixed at 3730 ppm/°C [66]. Empirical calculation for the convective and conductive heat transfer between the sensor surface and the air were performed as outlined in [11]. Heat losses through radiation were assumed to be negligible due to the fact that at operating temperatures of interest for SMO sensors, the convective and conductive heat losses to the air and conductive heat losses through the suspension beams are far more relevant [3,19,67]. For complete details on the geometry and fabrication of the two designs, as well as the electro-thermal simulations which includes the effects of conductive and convective heat losses, refer to [11].

3.2.2. The vacancy dynamics problem

The full sensor structures, shown in Fig. 1 are very complex, since they contain very thin layers, such as the microheater (200 nm) and very thick layers, such as the silicon wafer (700 m). Therefore, solving the vacancy dynamics problem for the full structure is not realistic, since the required mesh would need to be very fine, resulting in an unreasonable amount of nodes which have to be solved explicitly at all the time steps in the transient vacancy dynamics simulation. For this reason, we apply a hierarchical simulation approach: First, the full structure is meshed to solve only the electro-thermal problem in order to obtain the induced current density and temperature as well as their gradients. Subsequently, the transient vacancy dynamics model is applied on the membrane stack only, which includes the microheater and insulator, meaning that the silicon wafer, electrodes, and conducting pads have been removed. This simplification does not reduce the accuracy of the simulation output since the vacancy transport is only relevant inside the platinum microheater. In *sec*:appA this procedure is described in more detail. The model parameters used for the simulation of vacancy transport in the platinum film are provided in Table 1.

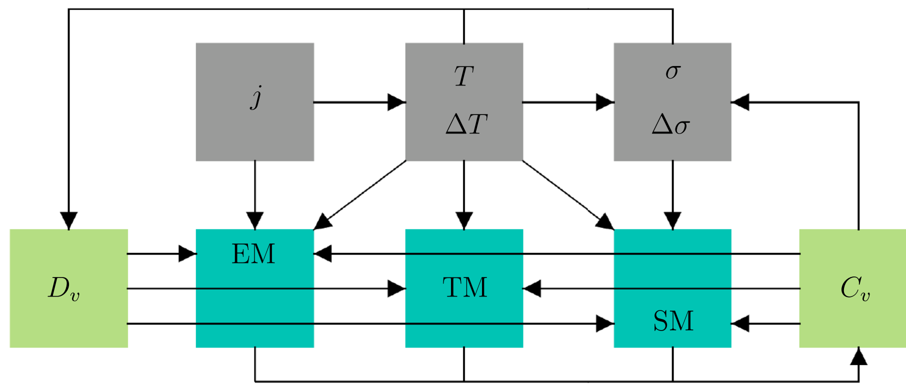

Fig. 3. Visual representation of the dependencies between EM, TM, and SM, their driving forces j, T, ΔT, σ, and $\Delta\sigma$, and the parameters of vacancy motion: diffusivity D_v and vacancy concentration C_v.

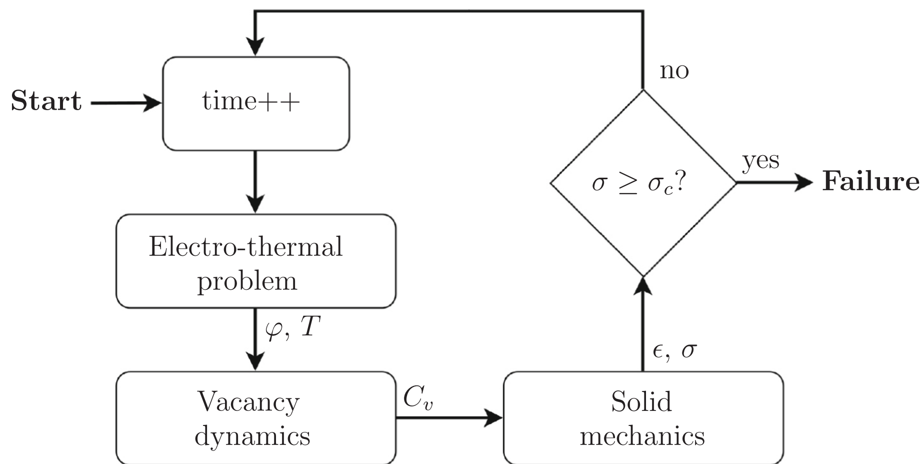

Fig. 4. Flowchart for modeling the vacancy-induced stress increase and ultimate failure in metal lines.

3.2.3. The solid mechanics problem

The increase and decrease in the vacancy concentration is accompanied by the development of compressive and tensile strains, respectively. The change in the vacancy-induced strain tensor ε over time t is given by

$$\frac{\delta\varepsilon}{\delta t} = \Omega\left[\Delta\cdot\overrightarrow{J_v} + f\frac{\delta C_v}{\delta t}\right] = \Omega\left[(1-f)\Delta\cdot\overrightarrow{J_v} + fG\right], \tag{7}$$

with f the vacancy relaxation factor (Table 1). The induced strain is directly proportional to the vacancy concentration, while the stress tensor is calculated assuming elasticity with the constitutive equation

$$\sigma_{ij} = C_{ijkl}\varepsilon_{kl}, \tag{8}$$

where C_{ijkl} is the stiffness tensor [68,69].

3.3. Simulation environment

All the simulations are performed using the finite element method implemented in COMSOL Multiphysics® [70]. The structures are meshed using first-order tetrahedral elements to represent the material volumes. The meshes of the full structure and the simplified membrane-only structure are provided in sec:appB. The simplified structure is used in order to allow for simulations with a denser mesh. As is always the case with simulations, there is a trade-off between accuracy and computational and memory efficiency. For the platinum microheater layer in both designs, an average tetrahedral element size and average volume of about 3 m and 0.26m^3, respectively, provided reasonable simulation times of several hours at each applied bias. In the membrane-only structure, this element size amounts to approximately 21,000 and 7700 mesh elements for the platinum microheater layer in the D1 and D2 designs, respectively. This translates to about 155,000 and 150,000 elements, for the entire membrane stack of the simplified structures. If this was to be extended to the full structure, about one million elements per design would be required. This is not an unreasonable amount to perform a stationary simulation, but for transient simulations, a smaller structure with less elements is preferred, especially when we aim to perform many simulation at various biases and temperatures.

In order to ensure that the simulations converge, special attention must be paid to the mesh element sizes and the time steps. Simulations will most often fail to converge if the time step is too large, meaning that the initial guess is too far from the expected result so that attempts to reach the equilibrium and find the solution will fail. This goes hand-in-hand with the mesh size: If the mesh elements are too large, then the gradients might be too large and may radically differ between neighboring elements, making it difficult to find the correct solution. For the initial time step, we choose a very small time on the order of 10^{-6} seconds, while the subsequent time steps are increased exponentially up to a maximum time step of 10^5 seconds.

4. Results and discussion

In order to assess the impact of vacancy-induced stress on platinum microheaters, the accelerated simulation condition must be defined. When regular operating temperatures between 300 °C and 550 °C for SMO gas sensors were used in the model, the simulations either did not

converge or they required very long and unrealistic run times. The most common reasons for non-convergence are that the initial time step is too large, and the equilibrium condition is thereby never found, or that the mesh is too coarse. However, since the simulations converge under accelerated conditions, the mesh is not a likely culprit here. Another concern here is that when forced to start with a very small time step, the simulation will require extremely long run times, which are unrealistic when trying to simulate many structures at different bias conditions. Accelerated conditions speed up the vacancy-induced effects, allowing to observe more impact for each time step, resulting in a shorter simulated time and thereby also in a reduced total simulation time.

To accelerate the model conditions, we increase the applied power by increasing the voltage difference between the microheater's conductive pads to levels which provide temperatures otherwise not reasonable in a physical device. The high applied power generates very high temperatures, up to about 1700 °C, which would otherwise induce quite significant internal deformation in the crystal structure of the platinum film, potentially result in atom diffusion across the dielectric, destroy the packaging and connecting wires, in addition to many other issues which would certainly destroy the device. However, our purpose is not to show the operational capability of these devices at such high temperatures, but rather to accelerate the EM and TM phenomena in the modeled devices, so as to enable reasonable simulation times. Effectively, we apply the accelerated conditions in lieu of a normalization factor to ensure that the simulations converge and can be performed as quickly as possible.

In order to ensure that the results can be extrapolated back to operating temperatures, the electro-thermal Joule heating problem is solved for by assuming only convective and conductive heat losses, as is expected is the case under normal operating conditions. The high power was applied by increasing the applied voltage, which then also induces high temperatures through Joule heating. Since, initially, the vacancy dynamics are driven solely by the temperature and voltage gradients, a relationship must exist between vacancy dynamics and the applied power. Furthermore, the simulation are performed at several applied powers ranging from about 20 mW to about 50 mW resulting in a wide range of high temperature conditions, from about 900 °C to 1700 °C. This wide range should allow us to examine the general relationship between the applied power/temperature and the vacancy-induced stress.

In Table 2 one set of electro-thermal simulation results for the platinum microheater layer of the two designs is summarized, in order to achieve the accelerated conditions for vacancy transport modeling. It is evident that the microheater array design (D2) has a much higher temperature gradient ∇T and a higher electric field $\nabla \varphi$ when compared to the dual-hotplate uniform temperature design (D1). This suggest that D2 will likely be more prone to early failure due to EM and TM. For both designs, the value of the temperature gradient is several orders of magnitude larger than the electric field, suggesting that TM might be more important than EM for these devices.

4.1. Vacancy transport in platinum microheaters

In order to quantify the impact of EM and TM on the vacancy transport mechanism, the induced forces in D1 are graphically represented in Fig. 5(a) and (b), respectively. Here, we note that the maximum TM force is slightly larger than the maximum EM force, while

Table 2
Relevant electrical and thermal results for the simulation of EM and TM in platinum microheaters.

	Power	Maximum value in Pt layer		
		T (°C)	∇**T** (K/m)	∇φ (V/m)
D1	38.8 mW	1664	1.69×10^{7}	1.75×10^{4}
D2	52.3 mW	1669	5.85×10^{7}	2.16×10^{4}

the location of the maxima are quite different. The EM force is highest at the corners, where the current density is also expected to be highest, while the TM force is highest around the edge of the microheater. After allowing the simulation to proceed for 10^8 seconds, the normalized vacancy concentration and stress distribution in the microheater are plotted, as shown in Fig. 5(c) and (d), respectively. The first observation is that the locations where the vacancy concentration and stress are negative (blue sections) correspond to the locations where the TM is largest. This means that the platinum atoms tend to move along the direction of the gradient from the hot to the cold side, similar to lead in solder joints [71], leaving behind vacancies at regions where the thermal gradient is large. The second observation is that the location with the highest stress (compressive, which is larger than tensile) and the largest accumulation of vacancies is the same as the location where the TM force is highest (top right edge of the microheater). This once again confirms that TM is a very significant phenomenon in these devices, likely more significant than EM.

In Fig. 6 we observe the same results on a microheater array structure, where high temperature gradients are an integral component of the design. Once again, the same observations made for the D1 design are also evident here, with the TM effect even more exacerbated. The compressive stress is also here larger than the tensile stress. Knowing that a high EM force results in a high tensile stress due to the creation of vacancies, the location where the compressive stress is high can be attributed to the TM force. In fact, when comparing Fig. 6(b) and (d) we note that the locations with the highest TM force are the same as the locations with the highest compressive stresses, respectively. This means that the TM and EM lead to compressive and tensile stresses, respectively, as suggested in Section 3.1 due to the positive valence of Pt atoms. and that the TM force's impact on vacancy migration must not be ignored. The maximum TM force is now five times higher than the maximum EM force, as can be observed from Fig. 6(b) and (a), respectively. The increased TM force also leads to a much higher vacancy concentration and stress accumulation, noted in Fig. 6(c) and (d), respectively. The compressive stress reaches several hundred MPa after a simulation of 10^8 seconds. This is a very large value and would very likely lead to cracking and failure in the platinum layer.

4.2. Vacancy concentration in platinum microheaters

In the previous section, the main forces acting on the vacancies were noted to be EM and TM. While this is true in the early stage of vacancy transport, eventually, SM becomes the main driving force during the later stages, as shown in Fig. 7 and observed in previous studies [72]. From Fig. 7 it becomes abundantly clear that the SM force is much higher for the microheater array design, once again solidifying our hypothesis that high thermal gradients have a significant impact in the overall vacancy transport and stress build-up in platinum microheaters. In the microheater array design D2, the stress-migration term in the later stages of vacancy transport reaches several tens of fN, while the dual-hotplate design D1 shows only a few fN. When this is compared with the EM and TM forces for the two designs, it is clear that the increased stress-migration is due to a faster vacancy dynamic transport under the influence of high temperature gradients or TM.

In Fig. 8 we observe how the maximum normalized maximum vacancy concentration ($C_v/C_{v0} - 1$) in the dual-hotplate platinum microheater design D1 (Fig. 1(a)) changes over time. Three steps in vacancy transport are quite clearly visible, as was observed in other metals [25,59]. The initial stage (until about 1s) is dominated by EM and TM, while the second stage (from about 1s until about 10^4s) is a quasi-steady state where the material's strain response balances the EM and TM forces. Finally, during the last stage (after about 10^4s), the rapid growth is induced by stress-migration [59,65,25]. By observing Fig. 7 it becomes quite evident that applying more power to the microheater, which increases the current density and temperature, results in an earlier spike in the SM force. From Fig. 8 it can further be observed that

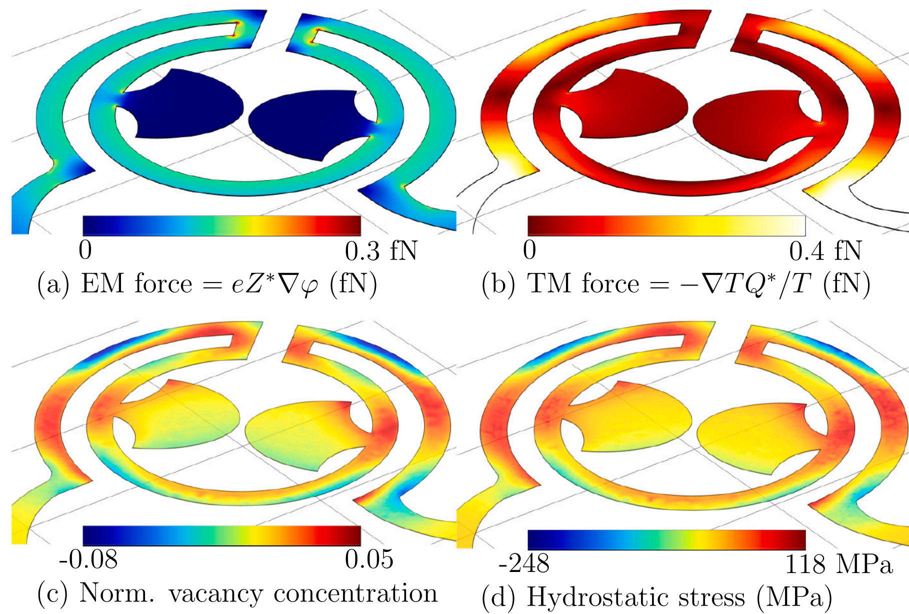

Fig. 5. Results of the simulation of vacancy-induced stress build-up in a highly uniform dual-hotplate platinum microheater (D1) after 10^8 seconds, when 38.8 mW are applied; (a) EM force; (b) TM force; (c) Normalized vacancy concentration (C_v/C_{v0}-1); (d) hydrostatic stress.

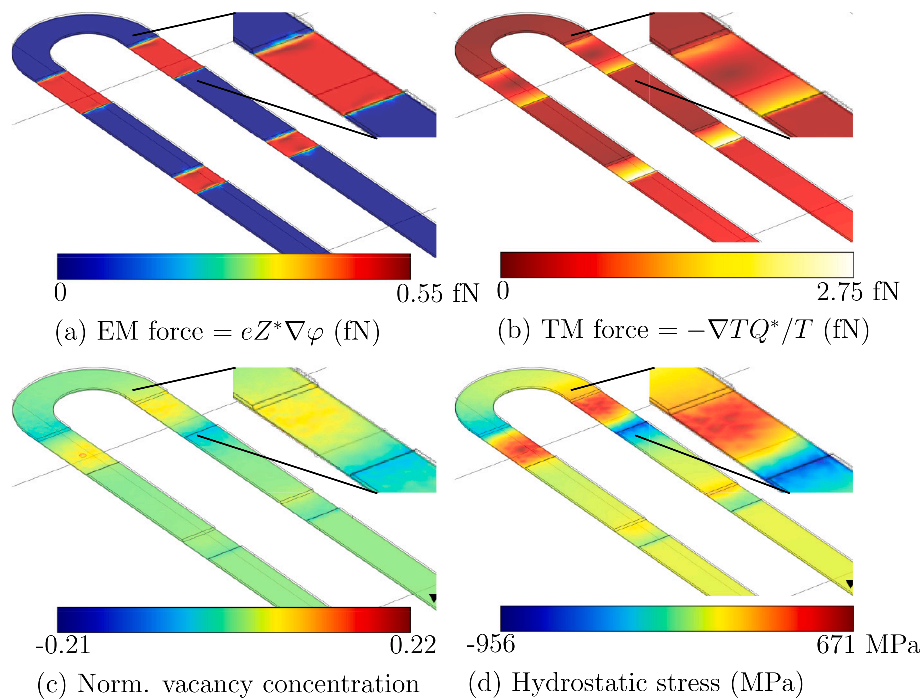

Fig. 6. Results of the simulation of vacancy-induced stress build-up in a platinum microheater array (D2) after 10^8 seconds, when 52.3 mW are applied; (a) EM force; (b) TM force; (c) Normalized vacancy concentration (C_v/C_{v0}-1); (d) hydrostatic stress.

this early SM activation cannot be attributed to the timing of the different stages, as they all seem to start the same approximate times. However, we note that the initial maximum normalized vacancy concentration, during the early stages which are dominated by EM and TM forces, are higher for microheater films which have a higher applied power and maximum temperature. Therefore, we can conclude that the initial response to the applied power and thermal gradient will play the most important role in the timing of the eventual vacancy-induced microheater failure.

4.3. *Vacancy-induced stress in platinum microheaters*

The evolution of the maximum tensile and compressive stresses observed over time in microheater design D1 and D2 are provided in Figs. 9 and 10, respectively. The first observation is that the stress curves' timing tends to follow the stress-migration forces, shown in Fig. 7. This once again confirms that the vacancy-induced stress follows the typical three-stage process, which is punctuated by the SM force. From what we know about the physics of vacancy transport and from Eqs. (2)–(6), once the stress becomes large, it leads to increased vacancy

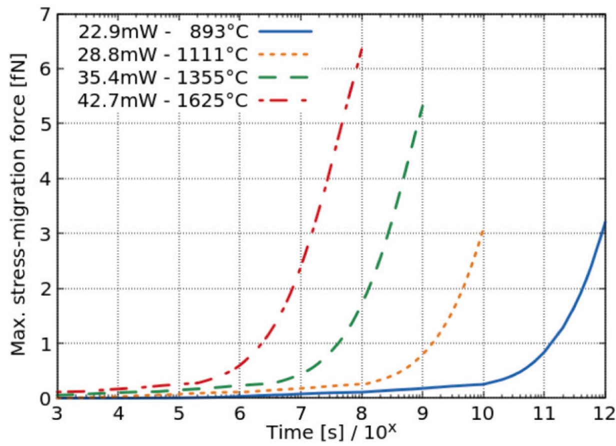

(a) Design D1: dual-hotplate

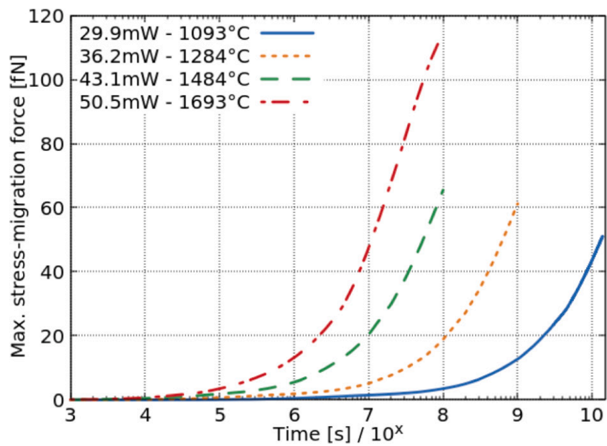

(b) Design D2: microheater array

Fig. 7. Maximum SM contributions to vacancy dynamics in the platinum-based microheater designs (a) D1 and (b) D2, from Fig. 1 with different applied powers and resulting maximum temperatures. It is evident that at later stages, the SM force surpasses the EM and TM forces of 0.3fN and 0.4fN in D1 and 0.55fN and 2.75fN in D2.

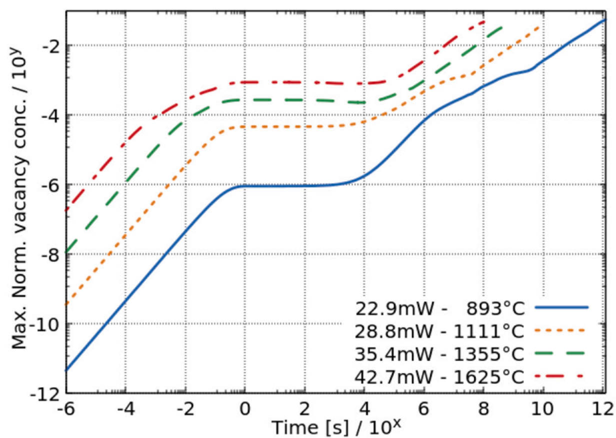

Fig. 8. Maximum normalized vacancy concentration ($C_v/C_{v0} - 1$) in the platinum-based microheater design D1 from Fig. 1(a) with different applied powers and resulting maximum temperatures.

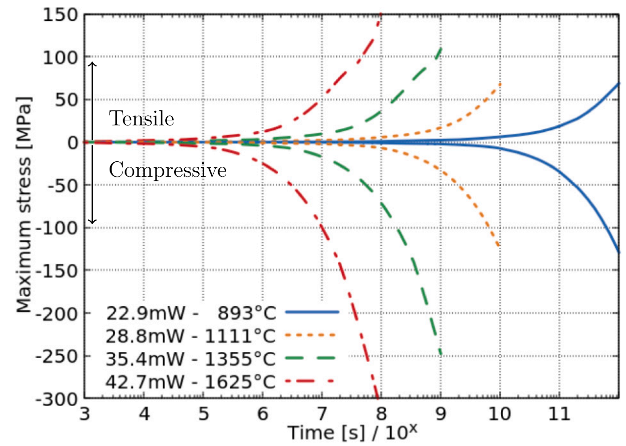

Fig. 9. Maximum tensile and compressive stresses (MPa) evolution in the platinum-based dual-hotplate uniform-temperature microheater design D1 from Fig. 1(a) with different applied powers leading to different maximum temperatures.

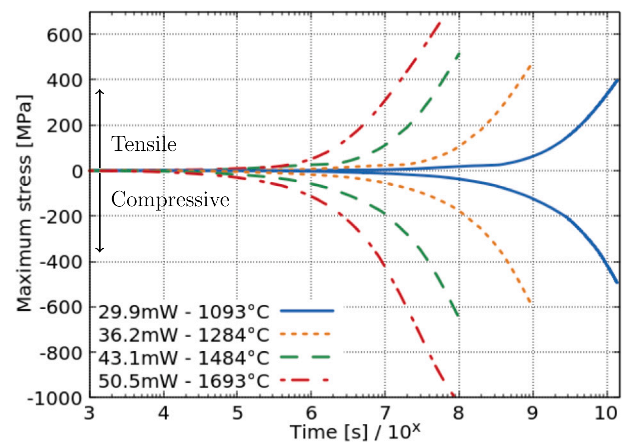

Fig. 10. Maximum tensile and compressive stresses (MPa) evolution in the platinum-based temperature array microheater design D2 from Fig. 1(b) with different applied powers leading to different maximum temperatures.

diffusion in Eq. (5) and an increased vacancy flux in Eq. (4). Both of these have the combined effect of creating more vacancies and causing more vacancy accumulation, further exacerbating the SM effect. So, SM increases vacancy accumulation, which increases SM; this cyclical and self-replicating effect is what leads to the high spike in the stresses after the SM force becomes significant enough, leading to eventual failure.

Another observation from Figs. 9 and 10 is that the maximum compressive stress is consistently higher than the maximum tensile stress by almost a factor of two. This is true for both designs under all simulation conditions, once again confirming the fact that the TM force is more important to vacancy transport and eventual high stress build-up than the EM force. This is backed by the observations in Figs. 5 and 6 showing the highest compressive stress at locations which also have the highest TM force. The observed stresses are on the order of several hundred MPa, which is quite high and could potentially be a contributing factor to sensor failure. The other factors to consider are the intrinsic stress and thermal stress due regular heating and cooling of the stacked layers, leading to membrane deflection and potential cracking [19,18,27,73]. It should be noted that ideally, in order for the as-fabricated membrane to be considered mechanically stable, its total intrinsic stress should not exceed 100 MPa [74,10]. Nevertheless, this value can be exceeded during operation due to the heating cycles and vacancy transport phenomena, discussed here. While there is no specific

stress value which immediately signals that a microheater has failed or cracked, in this study we chose a critical stress value of σ_c=100MPa in order to further observe how different operating conditions impact the stress build-up over time and eventual failure.

4.4. Mean-time-to-failure model for platinum microheaters

In order to generate a MTTF model for the two proposed microheaters, we set a critical stress value of 100 MPa to reflect the residual stress limitation. It should be noted that this value may not represent the real physical critical stress and this needs to be investigated further, especially since it also depends on how well the suspended membrane is able to elastically deflect in order to relax the stress. Nevertheless, whatever the value may be, the trend shown here is expected to be the same. Then, we observe the time t at which this level is reached under various applied conditions, meaning under varying applied powers and microheater temperatures. A plot of these results is given in Fig. 11. The first observation is that the microheater array design (D2) is more prone to failure since it requires much less time to reach the critical stress level. It is notable that the curves for both devices and their tensile and compressive behavior follow an Arrhenius expression

$$MTTF = A_0 exp\left(\frac{E_A}{kT}\right), \tag{9}$$

where the activation energy is given by E_A=2.85eV and the values of the pre-exponential factors A_0 are given in Table 3. This relation follows closely along Black's equation

$$MTTF = \frac{A_B}{j^n} exp\left(\frac{E_A}{kT}\right), \tag{10}$$

which is defined the same way with the only difference being that $A_0 \propto j^{-n}$ where n can be determined experimentally [64,68].

The parameters for the two designs are given in Table 3. We note that A_0 does not have a dependence on j, while Black's Law, in determining the MTTF, considers both the operating temperature and current density. However, contrary to this conventional wisdom, we note that the value of A_0 in these microheater designs does not change as we vary the applied bias. Rather, it changes for each design, meaning it depends on the geometry, and for each stress type. It is difficult to define the precise applied current density in our devices since we are no longer testing only EM along a single interconnect line with defined dimensions, but we are rather examining microheaters with complex curvatures. Nevertheless, in order to obtain the high temperatures, the applied power and thereby also the applied current were varied, while A_0 did not change. Due to the fact that A_0 remains constant under varying applied bias conditions (applied current density and microheater temperature), we can assume that neither the temperature gradient (TM) nor the current density (EM) significantly influence this parameter, unlike in Blacks' formulation from Eq. (10).

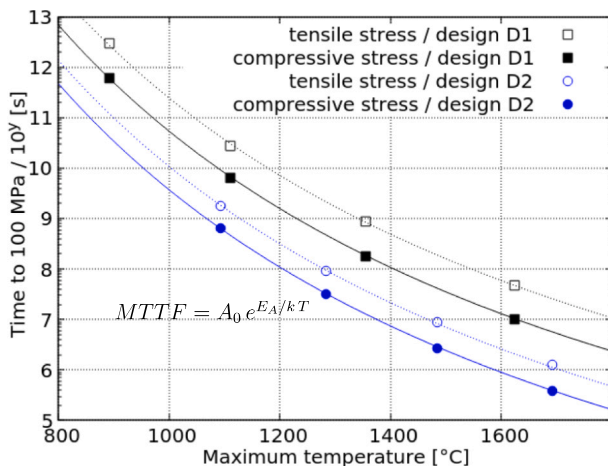

Fig. 11. Impact of the maximum temperature in the platinum microheaters on the time to reach 100 MPa tensile and compressive stress. The best-fit lines are Arrhenius expressions from Eq. (9) and Table 3.

Table 3
Calibrated parameters for the two studied microheater designs (Fig. 1) whose fit to simulation are shown in Fig. 11.

3*E_A	A_0			
	Design D1		Design D2	
	Tensile	Compressive	Tensile	Compressive
2.853 eV	1.25 s	0.275 s	55 ms	19 ms

The different values observed for the constant A_0 for the tensile and compressive stresses tends to suggest that the driving forces behind the two types of stresses are different. The fitted value for E_A shows that the dependence on temperature still holds from Black's equation, since the energy is the same for both designs and both stress types. Furthermore, since the value is a constant across several applied powers and current densities, the MTTF is effectively independent of the applied current density and thereby it is also independent of the EM force.

4.5. Extrapolation to operating conditions

Using the MTTF model from the previous section and observations from Fig. 11, we can determine the potential for platinum microheater failure during the operation of the proposed SMO sensor designs. For this, we will look at the compressive stress in the microheater array design (D2), which has the shortest MTTF of all the simulated setups. When this heater is operated at the envisioned temperature of 350 °C or at the SMO sensor relevant maximum temperature of 550 °C, the calculated MTTF is on the order of 10^{21} seconds or 10^{15} seconds, respectively. This means that it is highly unlikely that vacancy migration can have any significant effect on the operation of the proposed sensor designs. Only when we look at operation at extremely high temperatures, on the order of about 1500 °C do we get to MTTF times which could affect the sensors' reliability, in the range of 2.4×10^6 seconds. However, as mentioned earlier, at these high temperatures, many other phenomena will lead to failure in the platinum film long before TM will have any significant impact. Therefore, we can be reasonably confident that the designs we proposed are not at threat of early failure due to vacancy migration. However, this should be further studied with added insight from experimental measurements.

5. Conclusion

The necessity for CMOS integrated microheaters is highlighted by their application in the design of SMO gas sensors. Platinum is frequently used as the heater material due to its high melting point and resistance to oxidation at a broad range of temperatures. Nevertheless, in this study we examine the impact of EM and TM forces on the lifetime of novel proposed microheaters, intended for use in a low-power SMO sensor. We have shown that the TM force is much higher than the EM force, leading to high atom accumulation and compressive stresses in regions with high temperature gradients. The phenomenon is exacerbated in microheater arrays, where a temperature gradient is exploited to provide multiple temperatures in a single sensor. Furthermore, it was observed that the MTTF for platinum microheaters, which was determined to be the time required to reach a critical stress, follows an Arrhenius expression with an activation energy of 2.85 eV, independent of the heater's geometry. The pre-exponential constant is geometry dependent, but does not have a dependence on the current density or applied power. Finally, we show that these devices can achieve stresses

on the order of several hundred MPa when operating at physically unrealistic accelerated power and temperature conditions. However, when the MTTF is extrapolated back to normal operating conditions (up to 550 °C) we note failure times on the order of 10^{15} seconds, suggesting that the proposed designs are resistant to EM- and TM-induced failure.

CRediT authorship contribution statement

Dr. Lado Filipovic is the sole author and is therefore responsible for: Conceptualization; Data curation; Formal analysis; Funding acquisition; Investigation; Methodology; Project administration; Resources; Software; Supervision; Validation; Visualization; Writing.

Declaration of competing interest

The authors declare that they have no known competing financial interests or personal relationships that could have appeared to influence the work reported in this paper.

Acknowledgement

The authors acknowledge the TU Wien Bibliothek for financial support through its Open Access Funding Program.

Appendix A

As mentioned in Section 3.2.2, the vacancy dynamics problem is only solved for the membrane stack while the rest of the sensor structure is removed, including the silicon wafer, electrodes, and contact pads. This does not impact the results because our principal aim is to model the vacancy transport through the microheater, which is in its entirety located inside the membrane. The simulation, with an example using Design D2, proceeds as follows:

1. Solve the electro-thermal problem including Joule heating on the entire sensor structure by applying the appropriate voltage bias at the conductive pads. For example when we want to provide temperatures of 350 °C and 270 °C, we need to apply a bias of 0.25 V between the conductive pads in Design D2. In Fig. 12(a) we see the resulting temperature distribution.
2. To consider how to treat the simplified membrane-only simulation, we look at the voltage distribution inside the platinum layer of the full design in order to extract the voltages at the start of the membrane. The voltage through the platinum microheater layer in the full design is shown in Fig. 13 (a).
3. The voltages at the start of the membrane in the full design are then applied as inputs to the platinum microheater at the boundary for the membrane-only structure, as shown in Fig. 13(b). Using this structure as the input, the electro-thermal problem including Joule heating is once again calculated.

To make sure that the membrane-only structure provides the same behavior as the full structure, several items are characterized. A comparison between the full structure and the membrane-only structure regarding the provided sensor temperature is given in Fig. 12, showing no noticeable differences. For the platinum microheater itself, the potential, potential gradient, temperature, and temperature gradient are provided in Figs. 13, 14, 15, and 16, respectively. All the figures show that the simplified membrane-only structure successfully replicates the electro-thermal behavior of the full structure. Furthermore, from Fig. 12 we know to set the boundaries of the membrane to room temperature (20 °C).

When we look at the governing equations for vacancy diffusion in platinum (3) it is clear that everything is driven by the temperature T, temperature gradient ∇T, and potential gradient $\nabla \varphi$, while the other values are either global constants or material parameters. The stress gradient $\nabla \sigma$, on the other hand is initially negligible and is only increased under the changing vacancy concentration, driven by the initial temperature and potential distributions. Therefore, we are confident that the simplified membrane-only structure can sufficiently be used to simulate the vacancy transport of the platinum microheater sandwiched therein.

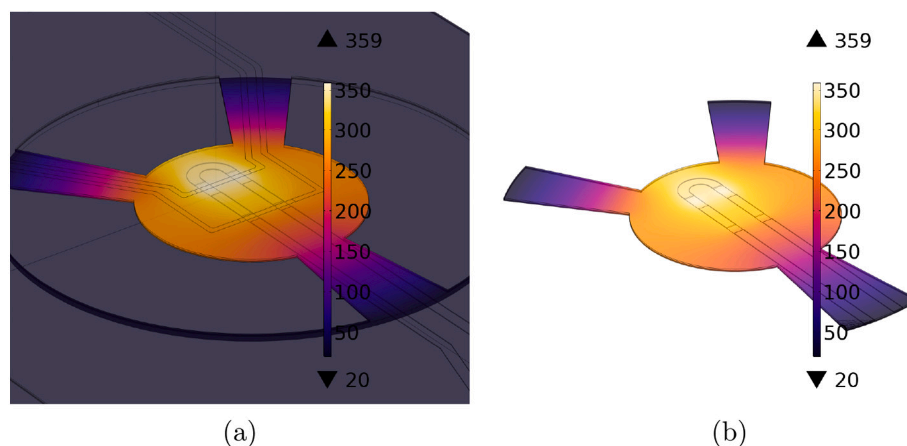

Fig. 12. Temperature (°C) provided by the presented sensor design D2 when (a) the full structure is simulated and a 0.25 V bias is applied and (b) when the membrane only is simulated and a 0.233 V bias is applied.

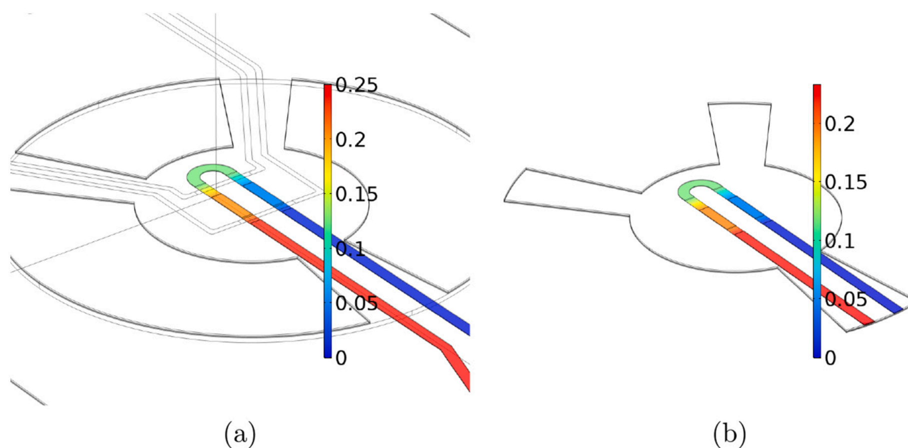

Fig. 13. Voltage (V) through the platinum microheater in design D2 when (a) the full structure is simulated and a 0.25 V bias is applied and (b) when the membrane only is simulated and a 0.233 V bias is applied.

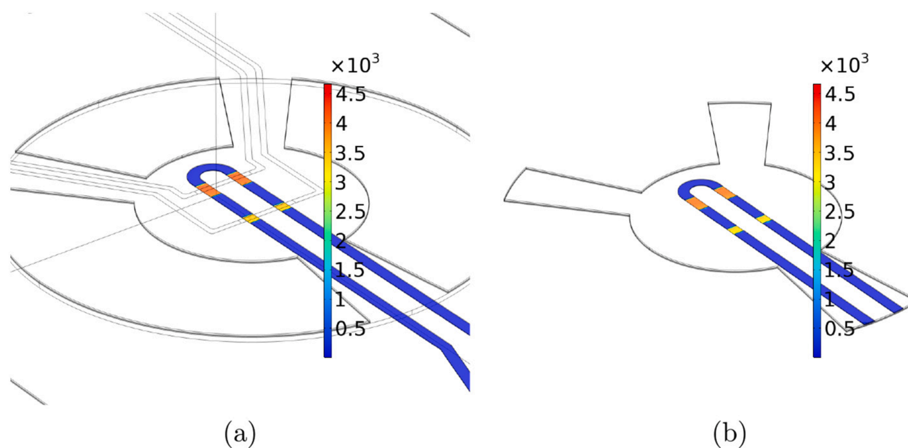

Fig. 14. Voltage gradient (V/m) through the platinum microheater in design D2 when (a) the full structure is simulated and a 0.25 V bias is applied and (b) when the membrane only is simulated and a 0.233 V bias is applied.

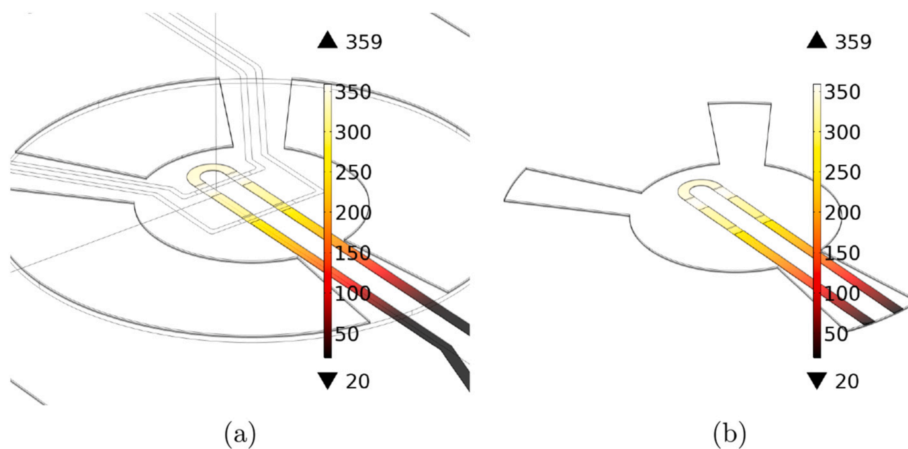

Fig. 15. Temperature (°C) through the platinum microheater in design D2 when (a) the full structure is simulated and a 0.25 V bias is applied and (b) when the membrane only is simulated and a 0.233 V bias is applied.

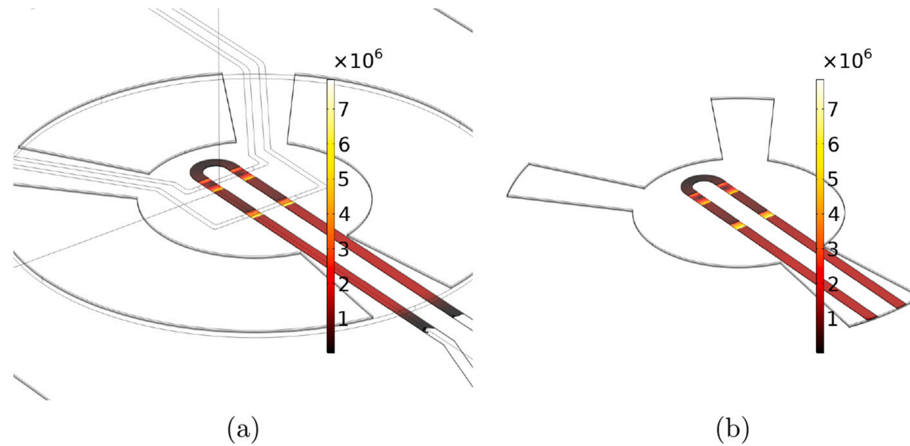

Fig. 16. Magnitude of the temperature gradient (K/m) through the platinum microheater in design D2 when (a) the full structure is simulated and a 0.25 V bias is applied and (b) when the membrane only is simulated and a 0.233 V bias is applied.

Appendix B

In this appendix, the meshed structures used in this study are provided. In Figs. 17 and 18 the meshed full and membrane-only structures of designs D1 and D2 are shown, respectively.

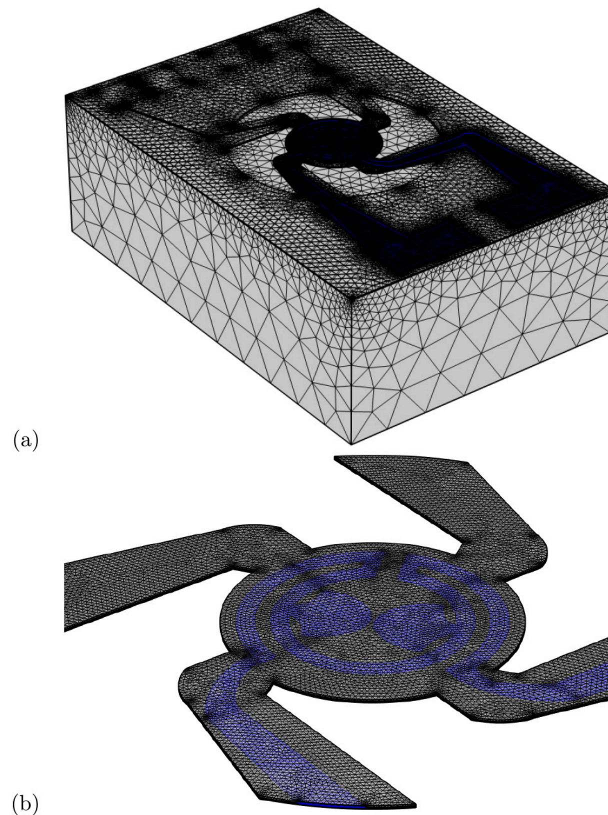

Fig. 17. Mesh of the sensor design D1 for the (a) full structure and (b) simplified membrane-only structure.

For design D1, the full structure contained 1.1 million tetrahedral elements, while the simplified structure contained about 155,000. The full structure required too much computational memory to be used for the transient simulation of the complete vacancy-induced stress. For design D2, the full structure contained 260,000 tetrahedral elements, while the simplified structure contained about 130,000 elements. The mesh used for the full structure was quite coarse and did not converge during transient simulations. Refining the mesh would result in too many mesh elements and the same computational memory problems noted with design D1.

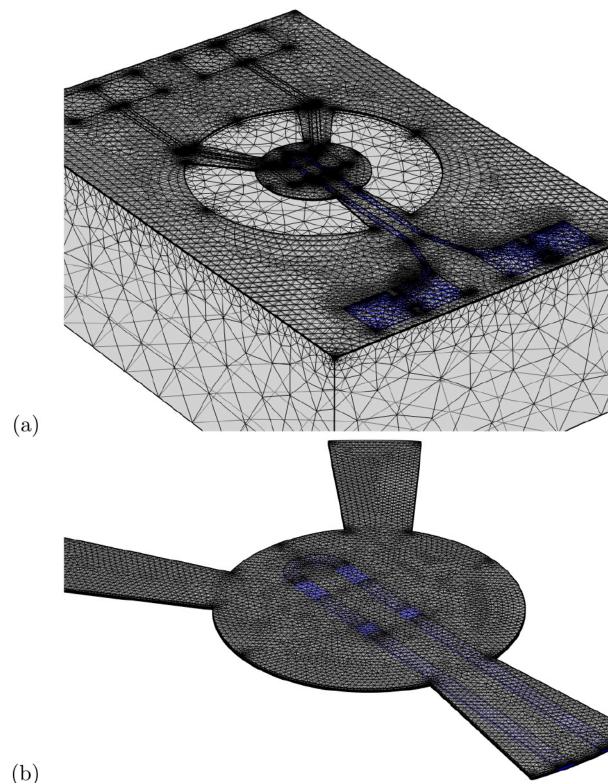

Fig. 18. Mesh of the sensor design D2 for the (a) full structure and (b) simplified membrane-only structure.

References

[1] A. Lahlalia, O.L. Neel, R. Shankar, S. Selberherr, L. Filipovic, Improved sensing capability of integrated semiconducting metal oxide gas sensor devices, Sensors 19 (2) (2019) 374-1–374-7, https://doi.org/10.3390/s19020374.

[2] A. Dey, Semiconductor metal oxide gas sensors: a review, Mater. Sci. Eng. B 229 (2018) 206–217, https://doi.org/10.1016/j.mseb.2017.12.036.

[3] S.K. Fung, Z. Tang, P.C. Chan, J.K. Sin, P.W. Cheung, Thermal analysis and design of a micro-hotplate for integrated gas-sensor applications, Sensors Actuators A Phys. 54 (1–3) (1996) 482–487, https://doi.org/10.1016/s0924-4247(97)80008-8.

[4] D. Bauer, M. Heeger, M. Gebhard, W. Benecke, Design and fabrication of a thermal infrared emitter, Sensors Actuators A Phys. 55 (1) (1996) 57–63, https://doi.org/10.1016/s0924-4247(96)01250-2.

[5] G.G. Helmut Budzier, Thermal Infrared Sensors, John Wiley & Sons, 2011.

[6] D. Popa, F. Udrea, Towards integrated mid-infrared gas sensors, Sensors 19 (9) (2019) 2076-1–2076-15, https://doi.org/10.3390/s19092076.

[7] F. Niklaus, C. Vieider, H. Jakobsen, MEMS-based uncooled infrared bolometer arrays: a review, in: J.-C. Chiao, X. Chen, Z. Zhou, X. Li (Eds.), Proc. SPIE: MEMS/MOEMS Technologies and Applications III 6836, SPIE, 2008, pp. 68360D-1–68360D-15, https://doi.org/10.1117/12.755128.

[8] U. Sassi, R. Parret, S. Nanot, M. Bruna, S. Borini, D.D. Fazio, Z. Zhao, E. Lidorikis, F. Koppens, A.C. Ferrari, A. Colli, Graphene-based mid-infrared room-temperature pyroelectric bolometers with ultrahigh temperature coefficient of resistance, Nature Commun. 8 (14311) (2017) 14311-1–14311-10, https://doi.org/10.1038/ncomms14311.

[9] D. Popa, S.Z. Ali, R. Hopper, Y. Dai, F. Udrea, Smart CMOS mid-infrared sensor array, Opt. Lett. 44 (17) (2019) 4111, https://doi.org/10.1364/ol.44.004111.

[10] L. Filipovic, A. Lahlalia, Review–System-on-chip SMO gas sensor integration in advanced CMOS technology, J. Electrochem. Soc. 165 (16) (2018) B862–B879, https://doi.org/10.1149/2.0731816jes.

[11] A. Lahlalia, L. Filipovic, S. Selberherr, Modeling and simulation of novel semiconducting metal oxide gas sensors for wearable devices, IEEE Sensors J. 18 (5) (2018) 1960–1970, https://doi.org/10.1109/JSEN.2018.2790001.

[12] S.Z. Ali, A.D. Luca, R. Hopper, S. Boual, J. Gardner, F. Udrea, A low-power, low-cost infra-red emitter in CMOS technology, IEEE Sensors J. 15 (12) (2015) 6775–6782, https://doi.org/10.1109/jsen.2015.2464693.

[13] A. Warren, A. Nylund, I. Olefjord, Oxidation of tungsten and tungsten carbide in dry and humid atmospheres, Int. J. Refract. Met. Hard Mater. 14 (5–6) (1996) 345–353, https://doi.org/10.1016/s0263-4368(96)00027-3.

[14] A.L. Purvis, B.M. Warnes, The effects of platinum concentration on the oxidation resistance of superalloys coated with single-phase platinum aluminide, Surf. Coat. Technol. 146–147 (2001) 1–6, https://doi.org/10.1016/s0257-8972(01)01362-7.

[15] J. Spannhake, A. Helwig, G. Faglia, G. Sberveglieri, T. Doll, T. Wassner, M. Eickhoff, G. MÃ¼ller, SnO: Sb – a new material for high-temperature MEMS heater applications: performance and limitations, Sensors Actuators B Chem. 124 (2) (2007) 421–428, https://doi.org/10.1016/j.snb.2007.01.004.

[16] R. Rusanov, H. Rank, T. Fuchs, R. Mueller-Fiedler, O. Kraft, Reliability characterization of a soot particle sensor in terms of stress- and electromigration in thin-film platinum, Microsyst. Technol. 22 (3) (2015) 481–493, https://doi.org/10.1007/s00542-015-2576-6.

[17] M. Prasad, D.S. Arya, V.K. Khanna, Fabrication and reliability study of a double spiral platinum-based MEMS hotplate, J. Micro/Nanolithogr. MEMS MOEMS 14 (2) (2015), https://doi.org/10.1117/1.jmm.14.2.025003.

[18] R.G. Spruit, J.T. van Omme, M.K. Ghatkesar, H.H.P. Garza, A review on development and optimization of microheaters for high-temperature in situ studies, J. Microelectromech. Syst. 26 (6) (2017) 1165–1182, https://doi.org/10.1109/jmems.2017.2757402.

[19] R. Coppeta, A. Lahlalia, D. Kozic, R. Hammer, J. Riedler, G. Toschkoff, A. Singulani, Z. Ali, M. Sagmeister, S. Carniello, S. Selberherr, L. Filipovic, Electro-thermal-mechanical modeling of gas sensor hotplates, in: Sensor Systems Simulations, Springer International Publishing, 2019, pp. 17–72, https://doi.org/10.1007/978-3-030-16577-2_2.

[20] Dec T.R. Mattsson, A.E. Mattsson, Calculating the vacancy formation energy in metals: pt, pd, and mo, Phys. Rev. B 66 (21) (2002), https://doi.org/10.1103/physrevb.66.214110.

[21] Y. Matsukawa, S.J. Zinkle, One-dimensional fast migration of vacancy clusters in metals, Science 318 (5852) (2007) 959–962, https://doi.org/10.1126/science.1148336.

[22] C. Chen, H. Tong, K. Tu, Electromigration and thermomigration in pb-free flip-chip solder joints, Annu. Rev. Mater. Res. 40 (1) (2010) 531–555, https://doi.org/10.1146/annurev.matsci.38.060407.130253.

[23] J. Lloyd, J. Clement, Electromigration in copper conductors, Thin Solid Films 262 (1–2) (1995) 135–141, https://doi.org/10.1016/0040-6090(94)05806-7.

[24] J. Tao, N. Cheung, C. Hu, Electromigration characteristics of copper interconnects, IEEE Electron Device Lett. 14 (5) (1993) 249–251, https://doi.org/10.1109/55.215183.

[25] L. Filipovic, A method for simulating the influence of grain boundaries and material interfaces on electromigration, Microelectron. Reliab. 97 (2019) 38–52, https://doi.org/10.1016/j.microrel.2019.04.005.

[26] L. Filipovic, Electromigration model for platinum hotplates, in: International Conference on Simulation of Semiconductor Processes and Devices (SISPAD), IEEE, 2020, pp. 315–318, https://doi.org/10.23919/sispad49475.2020.9241645.

[27] L. Filipovic, S. Selberherr, Thermo-electro-mechanical simulation of semiconductor metal oxide gas sensors, Materials 12 (15) (2019) 2410-1–2410-37, https://doi.org/10.3390/ma12152410.

[28] H. Low, M. Tse, M. Chiu, Thermal induced stress on the membrane in integrated gas sensor with micro-heater, in: Proceedings 1998 Hong Kong Electron Devices Meeting (Cat. No.98TH8368), IEEE, 1998, pp. 140–143, https://doi.org/10.1109/hkedm.1998.740206.

[29] P. Chaudhari, Grain growth and stress relief in thin films, J. Vac. Sci. Technol. 9 (1) (1972) 520–522, https://doi.org/10.1116/1.1316674.

[30] R. Hoffman, Stresses in thin films: the relevance of grain boundaries and impurities, Thin Solid Films 34 (2) (1976) 185–190, https://doi.org/10.1016/0040-6090(76)90453-3.

[31] M.F. Doerner, W.D. Nix, Stresses and deformation processes in thin films on substrates, Crit. Rev. Solid State Mater. Sci. 14 (3) (1988) 225–268, https://doi.org/10.1080/10408438808243734.

[32] E. Klokholm, B.S. Berry, Intrinsic stress in evaporated metal films, J. Electrochem. Soc. 115 (8) (1968) 823, https://doi.org/10.1149/1.2411441.

[33] E. Chason, B.W. Sheldon, L.B. Freund, J.A. Floro, S.J. Hearne, Origin of compressive residual stress in polycrystalline thin films, Phys. Rev. Lett. 88 (15) (2002), 156103, https://doi.org/10.1103/physrevlett.88.156103.

[34] B.W. Sheldon, A. Ditkowski, R. Beresford, E. Chason, J. Rankin, Intrinsic compressive stress in polycrystalline films with negligible grain boundary diffusion, J. Appl. Phys. 94 (2) (2003) 948–957, https://doi.org/10.1063/1.1575916.

[35] K. Cholevas, N. Liosatos, A. Romanov, M. Zaiser, M. Zaiser, E. Aifantis, E. Aifantis, Misfit dislocation patterning in thin films, Phys. Status Solidi B 209 (2) (1998) 295–304, https://doi.org/10.1002/(sici)1521-3951(199810)209:2<295::aid-pssb295>3.0.co;2-9.

[36] L. Dong, J. Schnitker, R.W. Smith, D.J. Srolovitz, Stress relaxation and misfit dislocation nucleation in the growth of misfitting films: a molecular dynamics simulation study, J. Appl. Phys. 83 (1) (1998) 217–227, https://doi.org/10.1063/1.366676.

[37] L. Filipovic, A.P. Singulani, F. Roger, S. Carniello, S. Selberherr, Intrinsic stress analysis of tungsten-lined open TSVs, Microelectron. Reliab. 55 (9–10) (2015) 1843–1848, https://doi.org/10.1016/j.microrel.2015.06.014.

[38] S.C. Seel, Stress and Structure Evolution During Volmer-Weber Growth of Thin Films, Massachusetts Institute of Technology, 2002.

[39] G. Adedokun, L. Geng, D. Xie, L. Xu, Low power perforated membrane microheater, Sensors Actuators A Phys. 322 (2021), 112607, https://doi.org/10.1016/j.sna.2021.112607.

[40] L. Filipovic, S. Selberherr, Processing of integrated gas sensor devices, in: TENCON 2015 – IEEE Region 10 Conference, IEEE, 2015, pp. 1–6, https://doi.org/10.1109/tencon.2015.7372781.

[41] A. Lahlalia, O.L. Neel, R. Shankar, S.Y. Kam, L. Filipovic, Electro-thermal simulation & characterization of a microheater for SMO gas sensors, J. Microelectromech. Syst. 27 (3) (2018) 529–537, https://doi.org/10.1109/jmems.2018.2822942.

[42] T.L. Anderson, Fracture Mechanics: Fundamentals and Applications, CRC Press/Taylor & Francis, Boca Raton, 2017.

[43] X.-K. Zhu, J.A. Joyce, Review of fracture toughness (G, K, J, CTOD, CTOA) testing and standardization, Eng. Fract. Mech. 85 (2012) 1–46, https://doi.org/10.1016/j.engfracmech.2012.02.001.

[44] O. Kolednik, Fracture mechanics, Am. Cancer Soc. (2012) 1–16, https://doi.org/10.1002/9781118097298.weoc096.

[45] A. Srivastava, Detection of volatile organic compounds (VOCs) using SnO gas-sensor array and artificial neural network, Sensors Actuators B Chem. 96 (1–2) (2003) 24–37, https://doi.org/10.1016/s0925-4005(03)00477-5.

[46] S.Y. Park, Y. Kim, T. Kim, T.H. Eom, S.Y. Kim, H.W. Jang, Chemoresistive materials for electronic nose: progress, perspectives, and challenges, InfoMat 1 (3) (2019) 289–316, https://doi.org/10.1002/inf2.12029.

[47] H. Ceric, H. Zahedmanesh, K. Croes, Analysis of electromigration failure of nano-interconnects through a combination of modeling and experimental methods, Microelectron. Reliab. 100–101 (2019) 113362-1–113362-6, https://doi.org/10.1016/j.microrel.2019.06.054.

[48] H. Ceric, S. Selberherr, Electromigration in submicron interconnect features of integrated circuits, Mater. Sci. Eng. R. Rep. 71 (5–6) (2011) 53–86, https://doi.org/10.1016/j.mser.2010.09.001.

[49] J.P. Dekker, A. Lodder, J. van Ek, Theory for the electromigration wind force in dilute alloys, Phys. Rev. B 56 (19) (1997) 12167–12177, https://doi.org/10.1103/physrevb.56.12167.

[50] M.A. Korhonen, P. Bo, K.N.Tu rgesen C.-Y. Li, Stress evolution due to electromigration in confined metal lines, J. Appl. Phys. 73 (8) (1993) 3790–3799, https://doi.org/10.1063/1.354073.

[51] V. Sukharev, E. Zschech, W.D. Nix, A model for electromigration-induced degradation mechanisms in dual-inlaid copper interconnects: effect of microstructure, J. Appl. Phys. 102 (5) (2007) 053505-1–053505-14, https://doi.org/10.1063/1.2775538.

[52] R. Rosenberg, M. Ohring, Void formation and growth during electromigration in thin films, J. Appl. Phys. 42 (13) (1971) 5671–5679, https://doi.org/10.1063/1.1659998.

[53] A. Seville, Effects of vacancies on the physical properties of platinum, Platin. Met. Rev. 19 (3) (1975) 96–99.

[54] F. Cattaneo, E. Germagnoli, F. Grasso, Self-diffusion in platinum, Philos. Mag. 7 (80) (1962) 1373–1383, https://doi.org/10.1080/14786436208213170.

[55] A. Zek, V. Doláková, A dilatometric study of platinum during repeated quenching, Czechoslov. J. Phys. 22 (4) (1972) 302–310, https://doi.org/10.1007/bf01689616.

[56] S. Ho, T. Hehenkamp, H. Huntington, Thermal diffusion in platinum, J. Phys. Chem. Solids 26 (2) (1965) 251–258, https://doi.org/10.1016/0022-3697(65)90152-6.

[57] A.H. Seville, Studies of the specific heat of platinum by modulation methods, Phys. Status Solidi A 21 (2) (1974) 649–658, https://doi.org/10.1002/pssa.2210210230.

[58] H. Ceric, R. Heinzl, C. Hollauer, T. Grasser, S. Selberherr, Microstructure and stress aspects of electromigration modeling, in: AIP Conference Proceedings 817, AIP, 2006, pp. 262–269, https://doi.org/10.1063/1.2173558.

[59] R. Kirchheim, Stress and electromigration in Al-lines of integrated circuits, Acta Metall. Mater. 40 (2) (1992) 309–323, https://doi.org/10.1016/0956-7151(92)90305-x.

[60] B.T. TrumiÄ‡, L.J. GomidÅ¾eloviÄ‡, S.R. MarjanoviÄ‡, V.R. KrstiÄ‡, Investigation of mechanical and structural characteristics of platinum and palladium at high temperatures, Rev. Metal. 51 (1) (2015) e038, https://doi.org/10.3989/revmetalm.038.

[61] J. Merker, D. Lupton, M. Topfer, H. Knake, High temperature mechanical properties of the platinum group metals, Platinum Metals Review(UK) 45 (2) (2001) 74–82.

[62] S. Collard, R. McLellan, High-temperature elastic constants of platinum single crystals, Acta Metall. Mater. 40 (4) (1992) 699–702, https://doi.org/10.1016/0956-7151(92)90011-3.

[63] J.R. Lloyd, Electromigration failure, J. Appl. Phys. 69 (11) (1991) 7601–7604, https://doi.org/10.1063/1.347529.

[64] J. Black, Electromigration failure modes in aluminum metallization for semiconductor devices, Proc. IEEE 57 (9) (1969) 1587–1594, https://doi.org/10.1109/proc.1969.7340.

[65] R. de Orio, H. Ceric, S. Selberherr, Physically based models of electromigration: from Black's equation to modern TCAD models, Microelectron. Reliab. 50 (6) (2010) 775–789, https://doi.org/10.1016/j.microrel.2010.01.007.

[66] N.H. Kim, D.M. Na, P.J. Ko, J.S. Park, W.S. Lee, Electrical and thermal properties of platinum thin films prepared by DC magnetron sputtering for micro-heater of microsensor applications after CMP process, Solid State Phenom. 124–126 (2007) 267–270, https://doi.org/10.4028/www.scientific.net/ssp.124-126.267.

[67] L. Filipovic, S. Selberherr, Stress in three-dimensionally integrated sensor systems, Microelectron. Reliab. 61 (2016) 3–10, https://doi.org/10.1016/j.microrel.2015.09.013.

[68] R. De Orio, H. Ceric, S. Selberherr, A compact model for early electromigration failures of copper dual-damascene interconnects, Microelectron. Reliab. 51 (9–11) (2011) 1573–1577, https://doi.org/10.1016/j.microrel.2011.07.049.

[69] O.C. Zienkiewicz, R.L. Taylor, The Finite Element Method for Solid and Structural Mechanics, Elsevier, 2005.

[70] COMSOL Multiphysics v. 5.5 COMSOL AB Stockholm, Sweden https://www.comsol.com/.

[71] W. Roush, J. Jaspal, Thermomigration in lead-indium solder, in: Proceedings of the 32nd Electronic Components Conference 32, 1982, pp. 342–345.

[72] I.A. Blech, Electromigration in thin aluminum films on titanium nitride, J. Appl. Phys. 47 (4) (1976) 1203–1208, https://doi.org/10.1063/1.322842.

[73] M. Rovitto, Electromigration Reliability Issue in Interconnects for Three-dimensional Integration Technologies, Ph.D. thesis, Technische Univesität Wien, 2016, https://www.iue.tuwien.ac.at/phd/rovitto.

[74] C. Rossi, P. Temple-Boyer, D. Estève, Realization and performance of thin SiO/SiN membrane for microheater applications, Sensors Actuators A Phys. 64 (3) (1998) 241–245, https://doi.org/10.1016/s0924-4247(97)01627-0.